Journal of Hydroinformatics

Journal of Hydroinformatics Vol 24 No 1, 179 doi: 10.2166/hydro.2022.134

Airborne LiDAR-assisted deep learning methodology for riparian land cover classification using aerial photographs and its application for flood modelling

Keisuke Yoshida [a,*], Shijun Pan [a], Junichi Taniguchi[b], Satoshi Nishiyama[a], Takashi Kojima[b] and Md. Touhidul Islam[a,c]

[a] Graduate School of Environmental and Life Science, Okayama University, Tsushima-naka 3-1-1, Kita-ku, Okayama 700-8530, Japan
[b] TOKEN C.E.E. Consultants Co., Ltd., Kita-Otsuka 1-15-6, Toyoshima-ku, Tokyo 170-0004, Japan
[c] Department of Irrigation and Water Management, Bangladesh Agricultural University, Mymensingh 2202, Bangladesh
*Corresponding author. E-mail: yoshida.k@okayama-u.ac.jp

KY, 0000-0002-8424-2271; SP, 0000-0002-3260-9019; MTI, 0000-0003-3206-0326

ABSTRACT

In response to challenges in land cover classification (LCC), many researchers have experimented recently with classification methods based on artificial intelligence techniques. For LCC mapping of the vegetated Asahi River in Japan, the current study uses deep learning (DL)-based DeepLabV3+ module for image segmentation of aerial photographs. We modified the existing model by concatenating data on its resultant output port to access the airborne laser bathymetry (ALB) dataset, including voxel-based laser points and vegetation height (i.e. digital surface model data minus digital terrain model data). Findings revealed that the modified approach improved the accuracy of LCC greatly compared to our earlier unsupervised ALB-based method, with 25 and 35% improvement, respectively, in overall accuracy and the macro F1-score for November 2017 dataset (no–leaf condition). Finally, by estimating flow-resistance parameters in flood modelling using LCC mapping-derived data, we conclude that the upgraded DL methodology produces better fit between numerically analyzed and observed peak water levels.

Key words: airborne laser bathymetry, deep learning, flow-resistance parameterization, riparian land cover classification, semantic segmentation

HIGHLIGHTS

- DeepLabV3+ model has been modified for ALB data application to riparian LCC mapping.
- Compared to the ALB-based method, the DL-based method is highlighted for distinguishing riparian vegetation species.
- Hydraulic parameters derived using DL-based LCC results were reasonably used for flood simulation.
- Our simulated water levels were much closer to field observations than those simulated using existing ALB-based methods.

INTRODUCTION

In recent years, climate change has led to frequent extreme and record-breaking flooding events worldwide. For instance, in mid-July 2021, European floods not seen in decades ravaged Germany, Belgium, and the Netherlands, killing hundreds of people and inundating villages and towns. Furthermore, China has been at high risk from disastrous flooding in 2020 (Wei *et al.* 2020). In fact, a flood struck Henan province of China in mid-July 2021. The severe rainfall constituted an average year's amount, but falling during just 3 days. It is noteworthy that, because of recent climate change, an extreme rainfall event struck western Japan, our study region, in early July 2018, causing flooding and sediment damage, inundating residential areas, and killing 81 people in Okayama prefecture (Yoshida *et al.* 2021). Researchers today are constantly confronted by new challenges posed by unprecedented river floods in such an ever-changing global hydrological environment (Global Floods 2021). Although riverbed excavation and embankment upgrading can be effective flood mitigation methods to address river flood control issues, the river's flow capacity in the current state must be assessed appropriately before either of these engineering terrain modifications can be implemented efficiently.

The important hydraulic engineering task of assessing flood capacity is based primarily on cross-sectional area changes and flow resistance factors (Shih & Chen 2021). In recent studies (e.g., Dimitriadis *et al.* 2016), researchers demonstrated through

benchmark simulations that the variability and uncertainty of flood propagation are primarily caused by channel geometry and roughness as compared to other factors such as inflow, longitudinal gradient, floodplain roughness, and model structure. Accordingly, on-site bed level surveys and land cover classification (LCC) mapping both play fundamental roles in quantifying such crucial parameters as attributable flow resistance. Especially for the case of vegetated streams, Green (2005) reported that total flow resistance is affected by Manning's roughness coefficients of the following factors: riverbed materials, surface irregularities, shape and size of the channel cross-section, obstructions, vegetation, channel meandering, and so on. In addition, Nikora *et al.* (2008) demonstrated that, in addition to stream dimensions, an excellent parameter for estimating hydraulic resistance is the spatial distribution of plant patches. However, regular field surveys of riparian vegetation properties are traditionally required for flood control exercises (Sun *et al.* 2010). In earlier cases, several river management projects were conducted, but strong emphasis was not placed on the spatial distribution of vegetation species and their height, although this task is now regarded as important in balanced river management (Nepf 2012). One practical approach for quantifying river channel and floodplain roughness is to use reference values related to flow resistance based on visual confirmation of aerial photographs, considering all factors affecting flow resistance (e.g. Chow 1959). However, this time-consuming, unrepeatable, and laborious method of actual measurement has been demonstrated to have limitations for large-scale use. Accordingly, accurate LCC mapping, including information of vegetation attributes, is necessary for balanced river management including measures such as flood risk and ecosystem management.

Over the years, remotely sensed technologies have proven to be effective for application to riparian vegetation attribute surveys, relying on the acquisition of stable digital surface model (DSM) and digital terrain model (DTM) data. For instance, Mason *et al.* (2003) used airborne laser scanning (ALS) to derive riparian vegetation heights for floodplain friction parameterization in hydrodynamic modelling. In addition, Straatsma & Baptist (2008) evaluated an ALS-based approach to derive hydrodynamically relevant surface features using multispectral data, demonstrating the importance of ALS for mapping vegetation height and for density attribution. Furthermore, Vetter *et al.* (2011) used dense ALS point cloud data to investigate the vertical vegetation structure for determining hydraulic roughness. More recently, airborne laser bathymetry (ALB) systems have been applied to acquire vegetation height and topo-bathymetric data (Yoshida *et al.* 2020), demonstrating superiority in collecting bed elevation data from submerged areas. Results show that ALB enables data collection on both land and underwater areas simultaneously. Although the ALB system has advantages for collecting underwater data, it also has shortcomings for collecting terrestrial data. For example, in dense vegetation, the near-infrared (NIR) laser used in ALB can penetrate the ground surface only ineffectively, resulting in a lack of laser points on the underlying structure (Tian *et al.* 2021). Because of this phenomenon, it is difficult for an unsupervised method using ALB data to distinguish between detailed species (e.g., woody vegetation and bamboo grove in our targeted vegetation). Furthermore, this method commonly depicts LCC mapping based on each specifically sized grid, such as the 2 m grid used in an earlier study (Yoshida *et al.* 2020), with no regard for the LCC of the surrounding grid. Such limitation produces a 'salt and pepper' effect (Blaschke *et al.* 2000; Yu *et al.* 2006) in LCC mapping, which strongly affects the accuracy of LCC prediction results. Furthermore, the existing method of manually setting thresholds (Do *et al.* 2019; Yoshida *et al.* 2020) for various parameters used in LCC (e.g., voxel-based points and vegetation height considered in our current study as discussed hereinafter) has drawbacks because the criteria or proposed values might differ greatly with different remotely sensed datasets. Because of these issues, it is crucially important to establish an appropriate approach to improve the accuracy of LCC predictions using ALB data.

More recently, a few fluvial researchers attempted to classify riparian vegetation with machine learning (ML) methods using only LiDAR point cloud (e.g. Fehérváry & Kiss 2020). For that approach, they used decision trees to identify each cell's land cover. Then they compared the results with a field survey of randomly selected cells. Although they identified LCCs with acceptable accuracy, the ML method used larger two-dimensional (2D) cells (e.g. 15 m$\times$15 m) to read the object's features, although each cell accommodated only one label for classification. In such a case, they might have a risk of missing out on other important land cover information. To overcome limitations of the earlier study, we intend to use a smaller square mesh of around 2 m in our current study. Furthermore, Carbonneau *et al.* (2020) attempted to assess LCC such as water, dry exposed sediment, green vegetation, senescent vegetation, and roads using red–green–blue (RGB) images from 11 rivers in different countries based on a modified model: 'convolutional neural network-supervised classification'. Their findings with higher identification accuracy might be beneficial for ecological conservation in fluvial environments. However, they did not test their results for flow-resistance parameterization attributable to riparian vegetation, which we are particularly addressing here for river flood flow simulation. In addition, the ML technique demonstrates its shortcomings in pixel-based image classification (i.e. LCC mapping), where complicated feature extraction is necessary (Dargan *et al.* 2019).

Furthermore, manual feature extraction (e.g. data analysis, interpretation) is necessary for ML methods, whereas automatic feature extraction functions have been used widely for deep learning (DL) (a type of ML) models in recent years, particularly for models with encoder–decoder modules. For instance, the DL image processing techniques of DeepLabV3+ (Chen *et al.* 2018) have demonstrated their benefits in overcoming challenges in semantic segmentation, while classic U-Net (Ronneberger *et al.* 2015) can also extract features from images using the familiar encoder–decoder structure as DeepLabV3+. However, the DeepLabV3+ model can extract features more efficiently when assisted by the atrous spatial pyramid pooling module (Chen *et al.* 2017). Therefore, for the first time, we used the DeepLabV3+ model (RGB) in conjunction with ALB-derived voxel-based laser points and vegetation height information to infer LCC mapping, demonstrating the novelty of our current study.

In early July 2018, our targeted study site, the vegetated lower Asahi River, Okayama prefecture, Japan, details of which are described hereinafter, was struck by extreme flooding with discharge of approximately 4,500 $m^3 s^{-1}$. Because of riparian vegetation such as heavy density of woody and bamboo groves, the studied river reached record water levels (Yoshida *et al.* 2021). Therefore, appropriate LCC mapping is necessary to estimate flow-resistance parameters attributable to riparian vegetation in flood modelling. In light of the issues described earlier, this study was conducted to examine a proposed DL-based methodology for LCC mapping in riparian areas considering ALB-derived voxel-based laser points and vegetation height. In the current study, ALB measurements include overland and underwater bed elevation surveys using near-infrared and green lasers. In addition, during the LiDAR campaigns, we captured aerial photographs and leveraged the RGB information to assess LCC using the current DL approach. Consequently, airborne surveys assist us in determining the flood flow capacity by providing bed elevation data and generating LCC mapping for use as inputs in numerical simulation. However, the new LCC mapping approach presented herein is particularly expected to perform better than earlier unsupervised methods (clustering) at distinguishing the most dominant riparian vegetation species (i.e. woody vegetation and bamboo grove) in our targeted area. Finally, the proposed LCC reasonably estimated spatially distributed hydrodynamic roughness in the 2018 Asahi River flood modelling. Overall, this study is expected to aid policymakers in developing a balanced scenario for both flood control and ecosystem management tasks while considering riparian LCC.

STUDY SITE AND METHODS

Study site

Figure 1(a) depicts our study site, which is located on the lower Asahi River, a Class I (state-controlled) river in Japan, flowing through Okayama prefecture into the Seto Inland Sea. The catchment area of the targeted river is 1,810 km^2. The average river discharge at the Makiyama hydraulic station, which is at the 20 kilometer post (KP) upstream of the targeted domain, was 57.12 $m^3 s^{-1}$ during 1965–2005 (MLIT 2007). Throughout this study, the KP value denotes the longitudinal distance (kilometre, km) from the targeted river mouth. Furthermore, the riverbed slope is approximately 1:600. The channel width is about 300 m in the targeted reach. The targeted domain was 13.2–17.4 KP, as shown in Figure 1(a) (right), for both the LCC and flood simulation cases. Furthermore, more recently, widely diverse vegetation has been visible at the targeted site, which has raised severe concerns about effective flood control and ecosystem management measures. Irrespective of those concerns, the riparian vegetation for the current LCC study is divisible into three types based on flow resistance: bamboo grove, herbaceous species (grass), and woody species (tree). Figure 1(b) represents the dense situation of riparian vegetation in our targeted river, which must be trimmed in a planned manner for flood control tasks, whereas riparian environment management, such as wildlife conservation, must be considered.

Data collection and processing

Data collection

For this study, we conducted ALB (Leica Chiroptera II; Leica Corp.) surveys in March, July, and November 2017 along a 6.2-km reach of the lower Asahi River (10.6–17.4 KP) controlled by the national government. As shown in Figure 1 (right), multiple flight operations were conducted in both leaf-off (March and November 2017) and leaf-on (July 2017) conditions to achieve overlapping coverage of the target area. The current system scanned the river channel for LCC using aircraft-mounted near-infrared and green lasers (Figure 2). The device commonly uses the green laser to detect underwater (bottom) surfaces because green light can penetrate the water column to some degree. By contrast, the near-infrared laser is used to detect terrain surfaces, including vegetation identification, because it is readily reflected by the air–water interface. The laser beam of this measurement device is specially processed, considering the refraction angle of the green laser at the air–water interface,

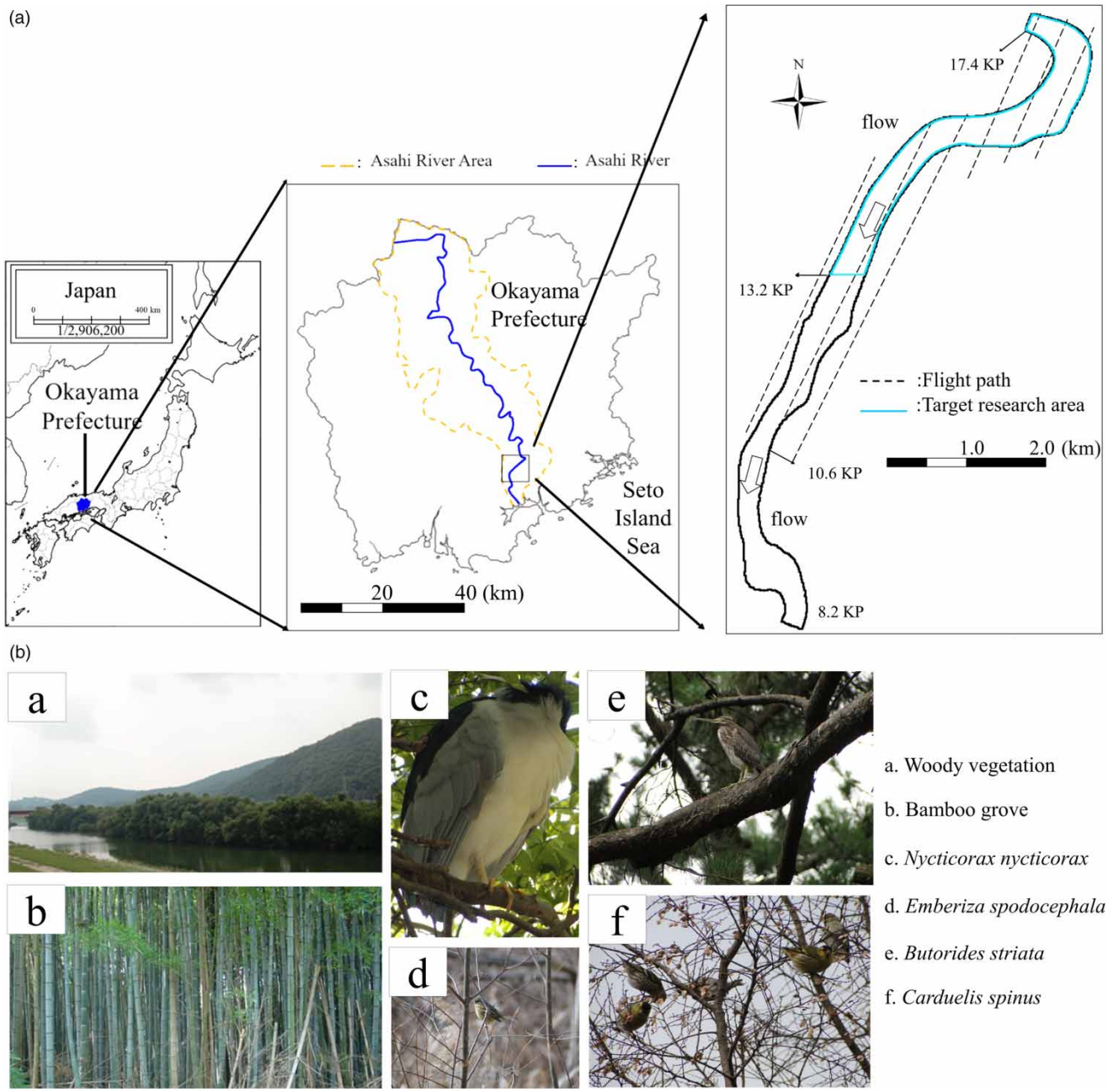

Figure 1 | Perspective of targeted research area: (a) location of the Asahi River in Japan with the kilometer post (KP) values representing the longitudinal distance (km) from the river mouth and (b) vegetation and birds' species in the targeted research area.

so that the laser incident at the air–water interface has an elliptical footprint (Figure 2). Moreover, during each ALB measurement, a digital camera mounted directly beneath the aircraft took aerial photographs of the target river. Table 1 shows specifications of the equipment, measurement parameters, and river water quality at the time of measurements. Because the magnitude of turbidity in a river can strongly affect the amount of light incident into the water column, its value was confirmed before each ALB measurement. The water quality of the three target periods was reasonable for measuring the underwater terrain surface.

Data processing

To remove tilt and relief effects, the aerial photographs were converted to orthophotos, as shown in Figure 3. Herein, the aerial photographs' overlap and side-lap ratios were respectively greater than 60 and 30%. As shown in Figure 4, aerial

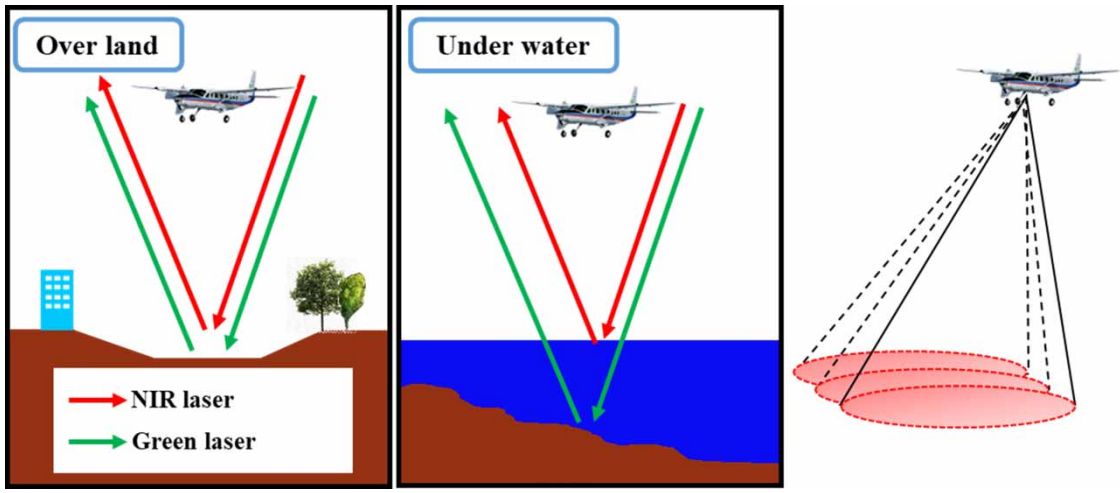

Figure 2 | Airborne laser bathymetry system using a NIR laser for overland surveys and a green pulsed laser for underwater surveys.

Table 1 | Specifications of the present ALB system and measurement conditions in the targeted river reach

Item			Measurement date of ALB and Aerial photograph		
			Mar. 2017	Jul. 2017	Nov. 2017
Equipment specifications	Laser wavelength range (nm)	NIR[a]	1,064	1,064	1,064
		Green	515	515	515
Measurement specifications	Number of laser beams (s^{-1})	NIR	148,000	148,000	148,000
		Green	35,000	35,000	35,000
	Ground altitude (m)		500	500	500
	Flight speed (km h^{-1})		220	220	111
	Density of measurement points (m^{-2})	NIR	9.0	9.0	18.0
		Green	2.0	2.0	4.0
Photograph specifications	Resolution (cm $pixel^{-1}$)		10	10	10
Water quality	Turbidity[b] (degree[c])		2.9	3.8	3.2

[a]Near-infrared.
[b]Ministry of Land, Infrastructure, Transport and Tourism hydrological water quality database (Asahi River, Otoide Weir).
[c]One degree of Japan Industrial Standard (JIS K0101) is the same as when 1 mg of standard substance (kaolin or formazine) is contained in 1 L of purified water.

photographs from 13.2 to 17.4 KP captured during the targeted three periods were processed sequentially using the four steps depicted in Figure 3. Figure 5 shows the ALB data processing, beginning with establishment of a Cartesian grid in the target domain comprising three-dimensional (3D) voxels. Each voxel, which has 0.5 m side length, can only hold one laser point data point using a filter to maintain uniform laser point density. In other words, we kept only the highest one from the ALB measurement rather than all the points for each voxel (Yoshida *et al.* 2017). For use as a parameter in subsequent 2D flood simulations, a horizontal 2D cell that can include all laser points in the processed 3D voxel was created. The points in each 2D cell are designated as voxel-based points (n). We identified the ground (riverbed or digital terrain model, DTM) after such processing by filtering the point cloud data near the lower part of the 2D cell. Later, we calculated the vegetation height (l) by locating the highest point in each 2D cell (digital surface model, DSM) after subtracting the DTM. Finally, as a reference for comparison, we attempted to define the LCC using an unsupervised approach (Yoshida *et al.* 2020), as shown in Table 2, based on the ALB data manipulations described above. In addition, because several bridges cross the Asahi River in the target region, data from the surrounding riverbed were used to approximate the bed height at the pier.

Processing of LCC mapping using the DL method

Mapping of the LCC using the DL method is divisible into two parts: data pre-processing and the processing using the modified DeepLabV3+ module. The true label (TL) and datasets were prepared in advance as input data for the following modules

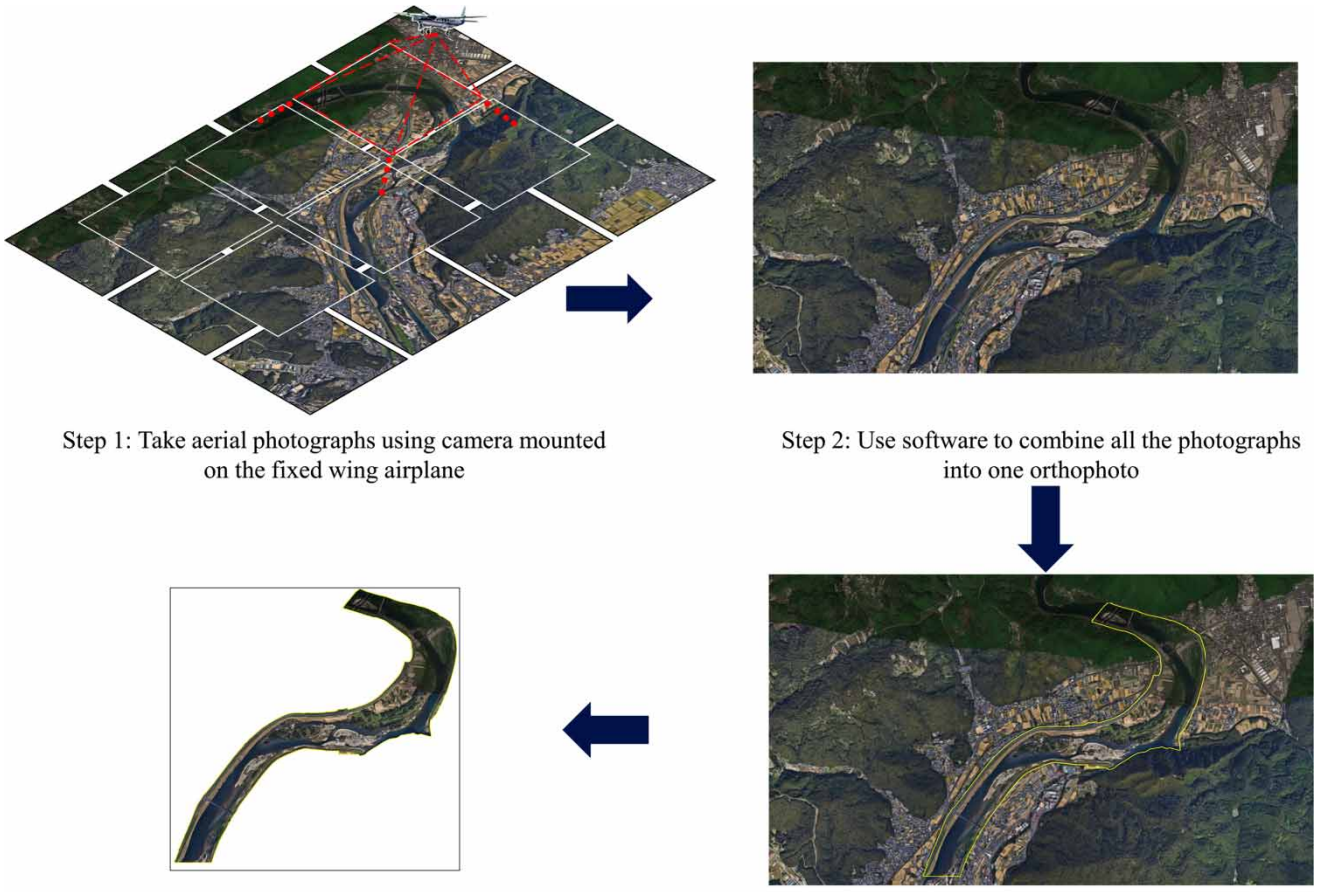

Figure 3 | Ortho-aerial photograph operation steps.

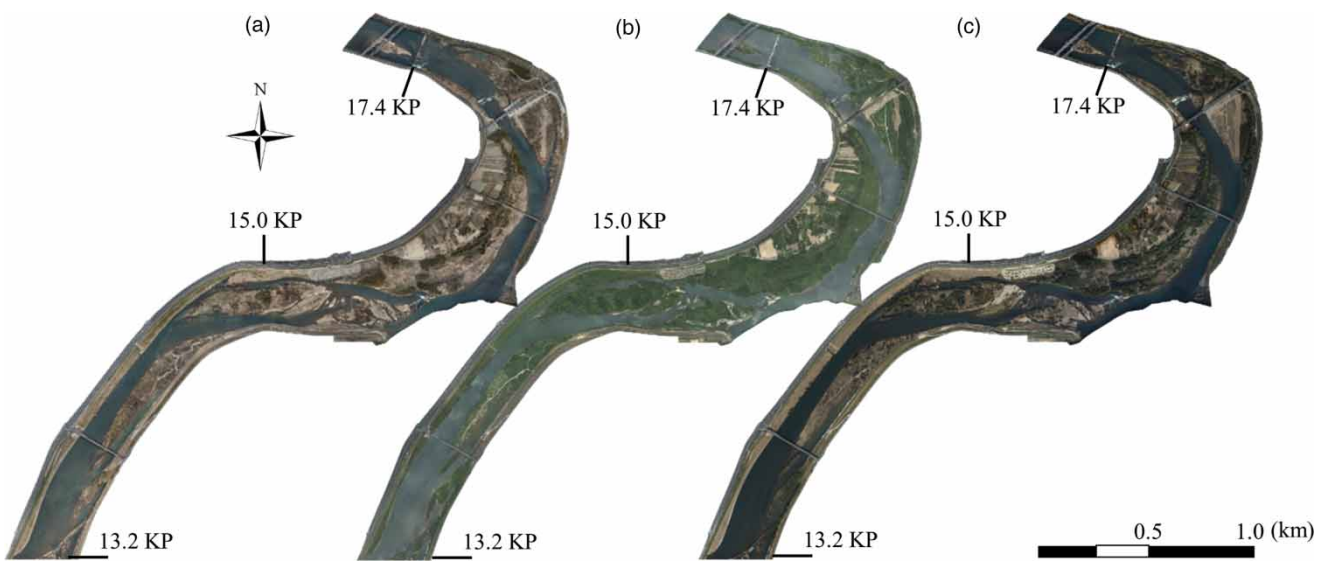

Figure 4 | Ortho-aerial photographs of the targeted area in (a) March, (b) July, and (c) November 2017.

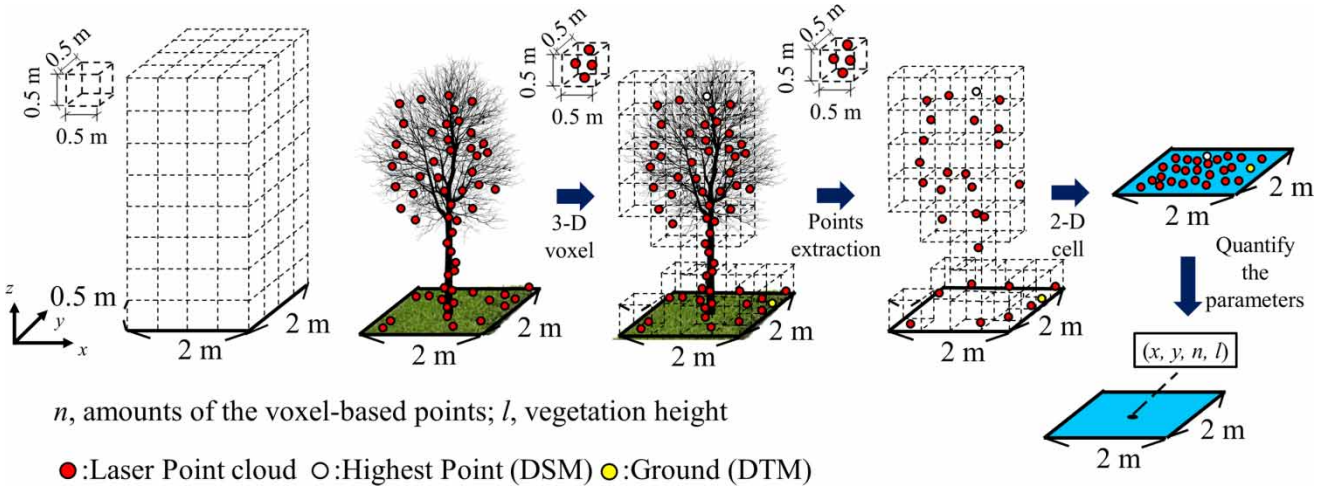

Figure 5 | Voxel-based ALB data processing.

Table 2 | LCC using ALB data with unsupervised method named as ALB-based LCC method

LCC	*n*	*l*
Bare ground	0	Under 30 cm
Tree	Over 13 points	Over 30 cm
Grass	Between 5 and 12 points	Over 30 cm
Water	0	0 cm
Bamboo[a]	–	–

[a]Bamboo is not distinguished for trees using the present ALB dataset (Yoshida *et al.* 2020).

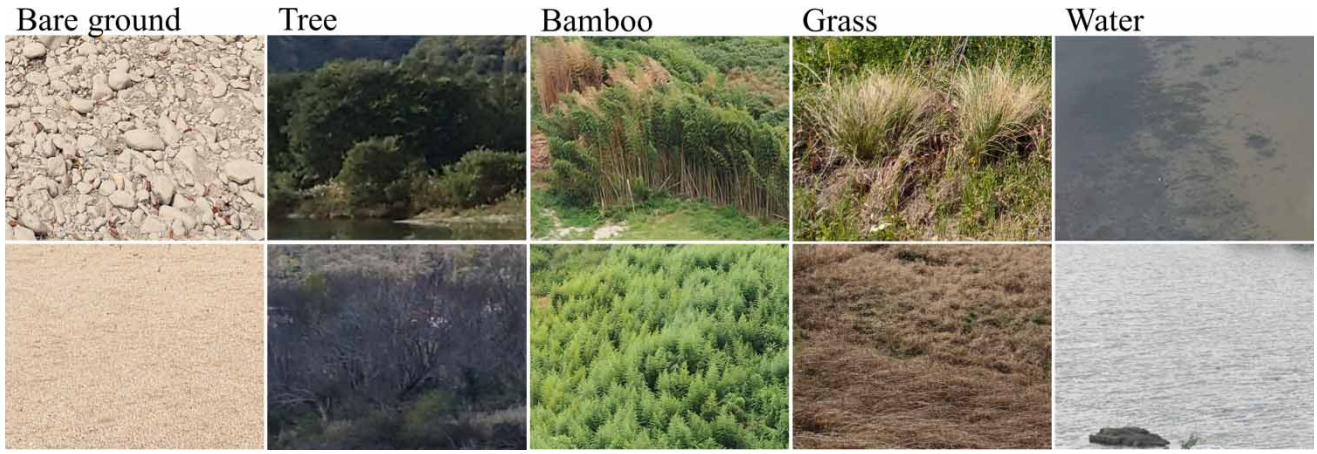

Figure 6 | Earlier field observation photograph samples of the targeted area for five typical categories of LCC.

during the pre-processing stage. In addition, the modified DeepLabV3+ module part is divisible into two sections: the conventional RGB-based method and the newly proposed RGB*nl*-based method. The RGB-based process uses only ortho-aerial photographs to train the DeepLabV3+ module and predict the LCC. By contrast, the RGB*nl*-based approach achieves some improvement by using ortho-aerial photographs, 2D voxel-based points n, and vegetation height l to train and predict the DeepLabV3+ module.

Pre-processing

In *mapping* the LCC pre-processing stage, we considered earlier field observation experience to obtain critical assistance in mapping the TL. As Figure 6 shows, earlier field observation photographs can provide information about the study target LCC characteristics such as texture and colour difference. Consequently, based on earlier field observations of our target area presented in Table 3, we roughly categorized the objects in the study area with five labels: bamboo, tree, grass, bare ground, and water. Furthermore, we sought to produce a rough distinction between natural and artificial areas in true label mapping. Therefore, aside from the five labels described above, we also considered the other two labels, such as 'road' and 'clutter' (i.e. all artificial objects except for roads), in the DL method's LCC mapping. Figure 7 presents an example of TL mapping based on orthophotos taken in November 2017.

Furthermore, some high-density areas of bamboo combined with some trees were noted in the targeted region. In orthophotos, trees with leaf-on conditions are difficult to distinguish from bamboo. In such cases, orthophotos from different periods must be compared to differentiate those targeted species. In contrast, 'grass' and 'trees' are more accessible to differentiation because of shadows and colour differences, which vary depending on the height difference between the two. It is noteworthy that, even in a leafless state, where 'grass' or 'bare ground' can be distinguished clearly under a 'tree', the area is still labelled as a 'tree' when the TL is drawn because regions that are too small during the deep learning process are not fully learned. For this study, we considered only mudflats and farmland as 'bare ground', which can be difficult to define. In addition, orthophotos include sufficient information to identify 'water', 'roads', and 'debris' (anthropogenic landscape components other than roads). Finally, it is noteworthy that our TL is based primarily on orthophotos. Therefore, we were unable to present information that existed but which was not represented in orthophotos (e.g. grass under a tree with leaves).

Based on the standards above, we labelled the land cover with seven labels for three periods of orthophotos of the target area, ranging from 13.2 to 17.4 KP, as shown in Figure 8. As an example, Figure 9 depicts a dataset from March 2017. Datasets (true labels, ortho-aerial photographs, and ALB dataset) from March were divided into three parts: (a) approximately 80% of the dataset for training, (b) approximately 10% of the dataset for validation, and (c) the remaining 10% of the dataset for testing. Datasets for the other two periods (July and November 2017) were assigned similarly. For this study, the modified module chose spatial resolution ratio of 1:10 between the ortho-aerial photographs and the ALB datasets based on DeepLabV3+ model specifications and data resolution. Accordingly, we set the spatial resolution for the ortho-aerial photographs to 0.2 m pixel^{-1} and for the ALB data to 2 m pixel^{-1}. Figure 10 depicts workflows in which ortho-aerial photographs and ALB datasets are cut into small panels using the above scales for pre-processing.

Processing of LCC mapping using the modified DeepLabV3+ module

The original DeepLabV3+ module extracts features from ortho-aerial photographs using an 'encoder–decoder' structure. The model's parameters are then optimized using TL. Subsequently, these parameters are saved as a 'trained model'. This training procedure determines the relations among input data, such as photographs, and the TL. Throughout this study, this processing was designated as the RGB-based LCC method. Later, this technique was upgraded by including an additional module

Table 3 | Previous field observation results for the targeted area

Items (labels)	Objects
A. Bamboo	Moso bamboo, Japanese timber bamboo
B. Tree	*Salix eriocarpa*, *Salix chaenomeloides*, *Ulmus parvifolia* *Juglans mandshurica* var, *Aphananthe aspera* *Quercus variabilis*, *Rhus javanica*, *Melia azedarach* *Robinia pseudoacacia*, Persica, Citrus, *Diospyros kaki*, etc.
C. Grass	*Phragmites australis*, *Miscanthus sacchariflorus* *Miscanthus sinensis*, *Phragmites japonica* *Typha domingensis*, *Ambrosia trifida*, *Pleioblastus simonii*, *Eragrostis curvula*, *Rosa multiflora*, Planted turf, etc.
D. Bare ground	Shoal, Road, Construction site, Agriculture ground
E. Water	Shallow water, Deep water

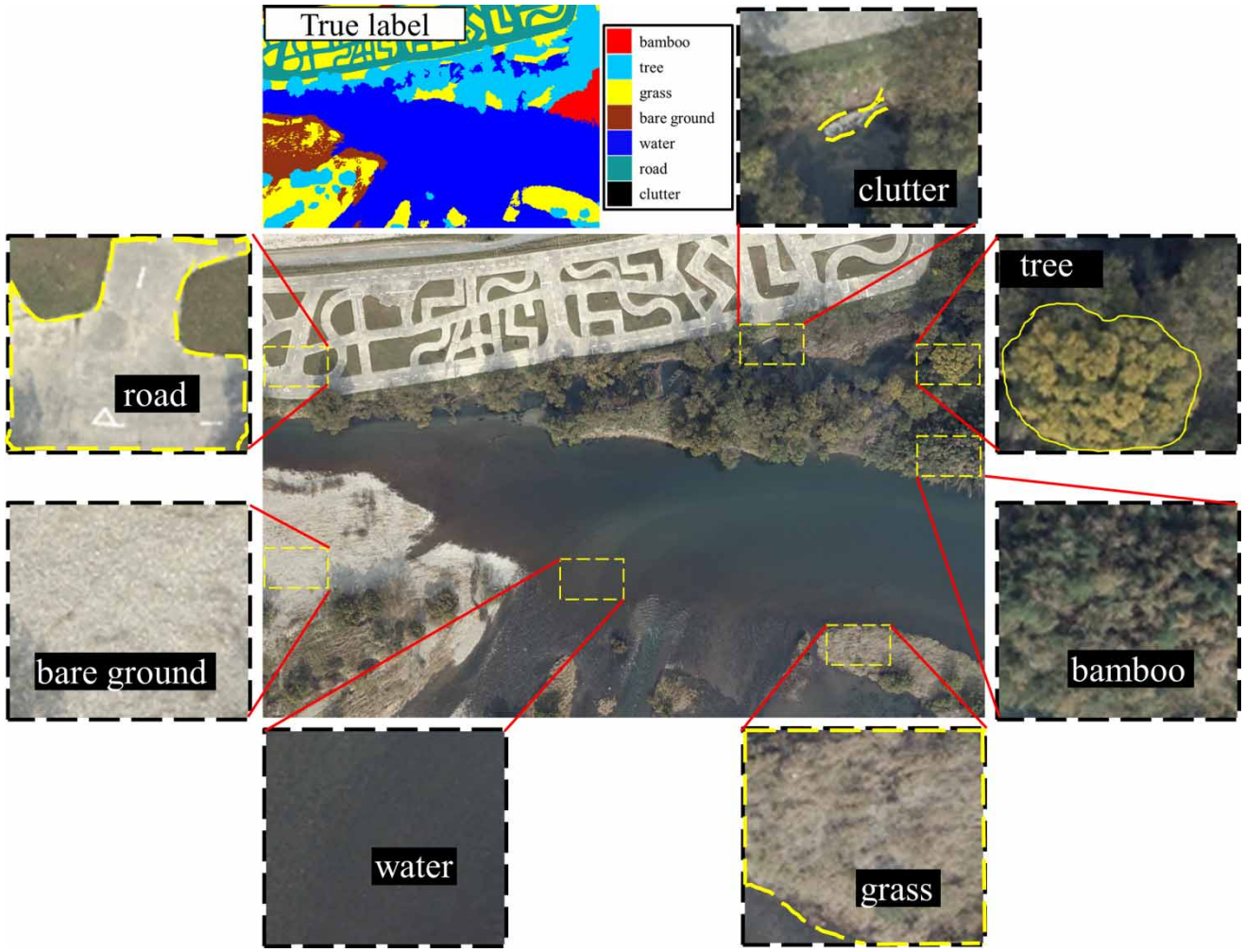

Figure 7 | Sample of true label mapping in November 2017.

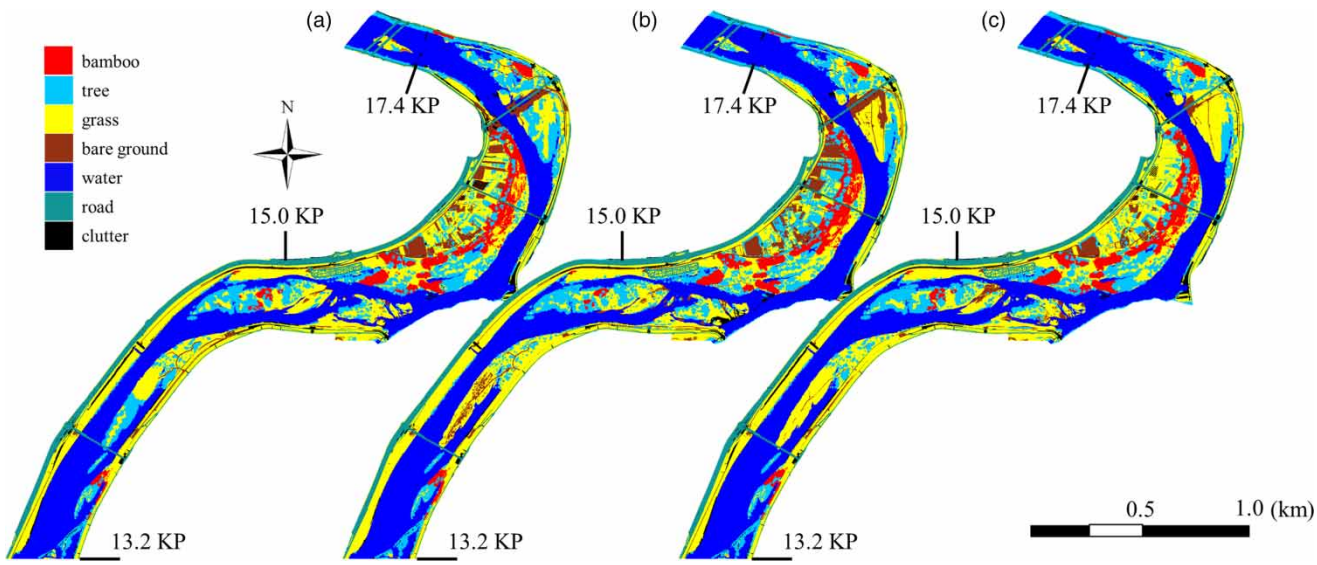

Figure 8 | True label mapping for the three targeted periods: (a) March, (b) July, and (c) November 2017.

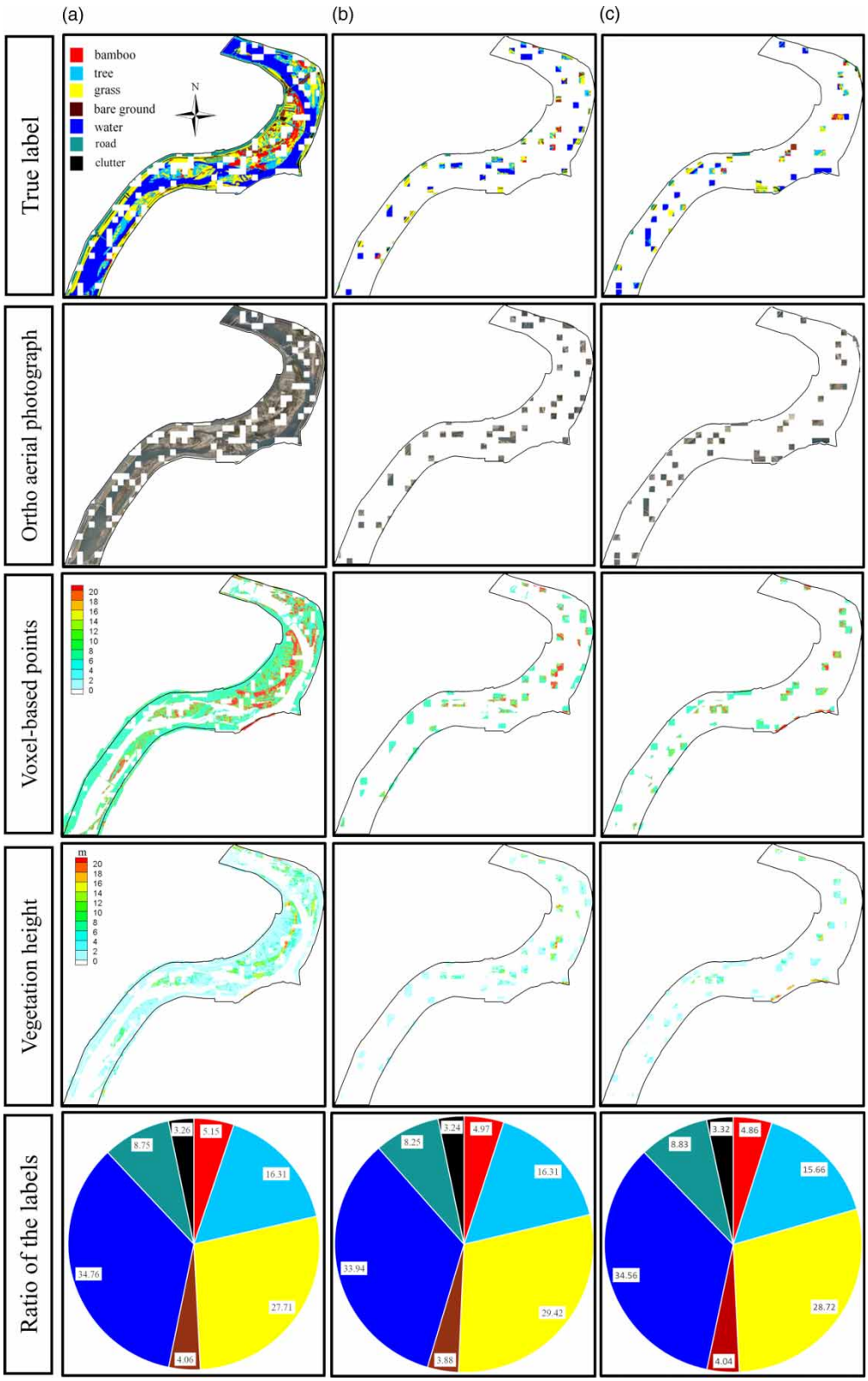

Figure 9 | Spatial distribution of the dataset in the (a) training, (b) valid, and (c) test areas (March 2017 dataset as example).

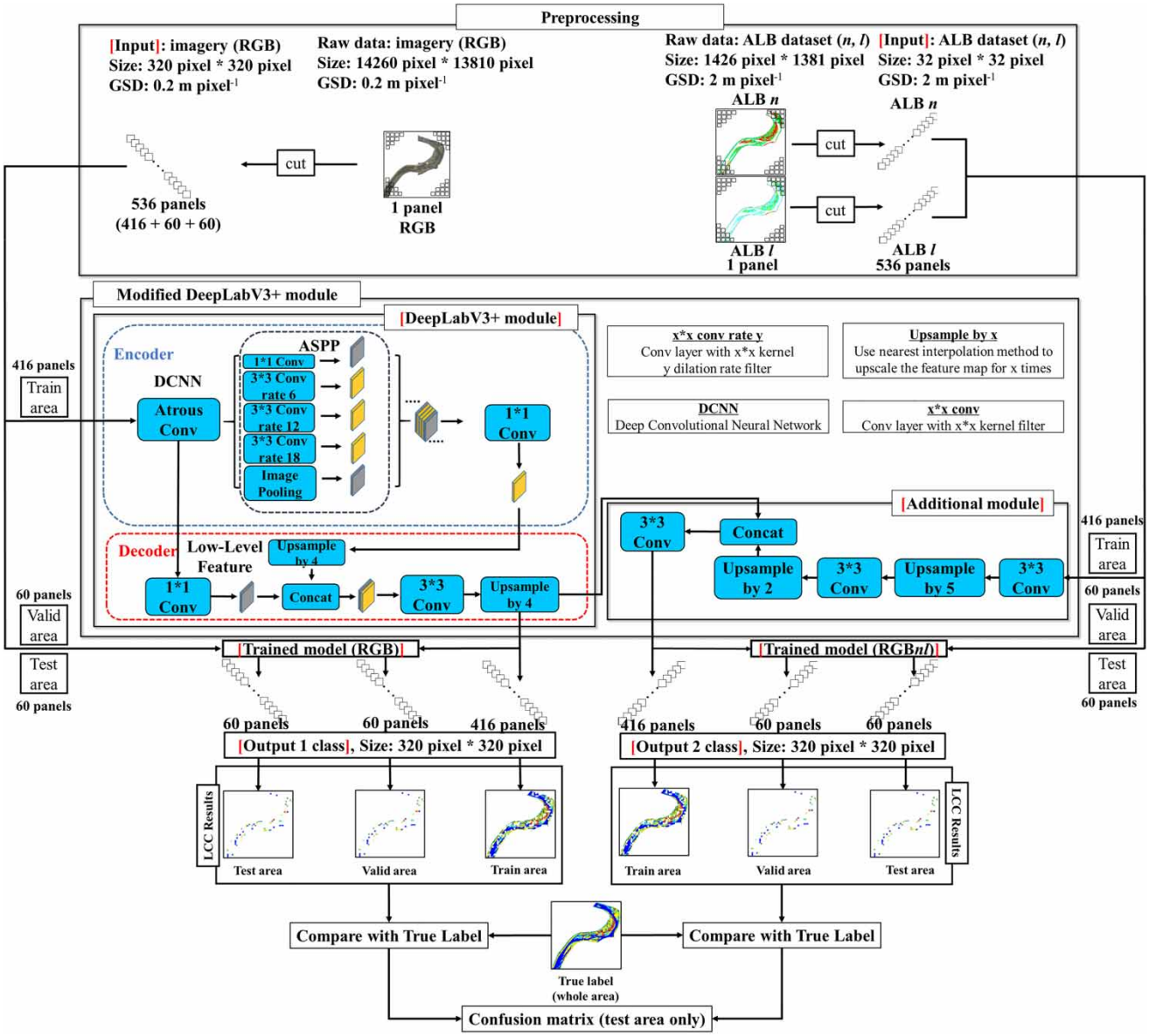

Figure 10 | Processing of mapping LCC with two DL methods.

with a 'decoder' function using the ALB dataset. To combine with the RGB-based 'trained model', the ALB dataset was expanded twice by factors of 2 and 5 in the additional module. Subsequently, we performed upsampling using an imaging technique called 'nearest-neighbor interpolation'. Then, we chose *n* and l as input data for the additional module for the ALB dataset. The parameters were optimized with the same TL as the RGB-based LCC method. This processing method was designated for this study as the RGB*nl*-based LCC method. The upgraded method's goal is to incorporate ALB data into the model to improve the accuracy of the inference results. Figure 10 depicts the workflows used for the processing of LCC mapping with the modified DeepLabV3+ module. The RGB-based method used for this processing is traced roughly as (a) training phase – [RGB image as input]→[DeepLabV3+ model]→[trained model] and (b) inference phase – [RGB image as input]→[trained model]→[LCC as output class 1]. By contrast, the RGB*nl*-based method image processing is represented as (a) training phase – [RGB image and ALB dataset as input]→[upgraded model]→[trained upgraded model] and (b) inference phase –[RGB image and ALB dataset as input]→[trained upgraded model]→[LCC as output class 2]. Finally, Table 4 presents a summary of the all training environment parameters used for programming.

Table 4 | Data training environment parameters and model setting of the DL methods

Developing environment							Model setting	
OS	GPU	GPU memory	GPU driver	CUDA	cuDNN	Framework	Epoch	Batch size (number of panels)
Ubuntu 20.04	GeForce RTX3090	24GB	Ver.460.39	Ver.11.2	8.04	Tensor-flow Ver.2.4.0	400	8

Table 5 | Analysis conditions of the train, valid and test data in March, July, and November 2017 using RGB- (Case 1) and RGB*nl*-based (Case 2, Case 3) methods

	Train data	Valid data	Test data		Train data	Valid data	Test data
Case 1-1	Mar. 2017 RGB		Mar. 2017 RGB	Case 2-1	Mar. 2017 RGB		Mar. 2017 RGB+ALB
Case 1-2			Jul. 2017 RGB	Case 2-2			Jul. 2017 RGB+ALB
Case 1-3			Nov. 2017 RGB	Case 2-3			Nov. 2017 RGB+ALB
Case 1-4	Jul. 2017 RGB		Mar. 2017 RGB	Case 2-4	Jul. 2017 RGB		Mar. 2017 RGB+ALB
Case 1-5			Jul. 2017 RGB	Case 2-5			Jul. 2017 RGB+ALB
Case 1-6			Nov. 2017 RGB	Case 2-6			Nov. 2017 RGB+ALB
Case 1-7	Nov. 2017 RGB		Mar. 2017 RGB	Case 2-7	Nov. 2017 RGB		Mar. 2017 RGB+ALB
Case 1-8			Jul. 2017 RGB	Case 2-8			Jul. 2017 RGB+ALB
Case 1-9			Nov. 2017 RGB	Case 2-9			Nov. 2017 RGB+ALB
				Case 3-1	Mar. 2017 RGB+ALB		Mar. 2017 RGB+ALB
				Case 3-2	Jul. 2017 RGB+ALB		Jul. 2017 RGB+ALB
				Case 3-3	Nov. 2017 RGB+ALB		Nov. 2017 RGB+ALB

APPLICATION

Comparisons of LCC mapping

To compare ALB-based LCC mapping, designated as Case 0, to DL method-based LCC mapping, both the whole area and the test area must be evaluated. We herein set the datasets into three cases to assess the RGB-based and RGB*nl*-based results, as presented in Table 5. Case 1 employs RGB data, whereas Cases 2 and 3 use combined data, including RGB data and the ALB dataset. The difference between Cases 2 and 3 is the input-to-output data ratio, with Case 3 having a larger input dataset. Especially, we aim at confirming two points: (a) whether or not more training data improve inference results and (b) versatility in training and inferring data from different periods. Finally, the confusion matrix (CM) and some indexes were used to assess the relative performance of the RGB-based and RGB*nl*-based methods.

Case 0: ALB-based method

First, as presented in Figure 11, we visually compared the LCC mapping based on the ALB-based method result, the DL method results, and the TL in November 2017. Because the ALB-based method can only segment five labels without 'road' and 'clutter', DL methods must also adhere to this rule, with 'road' and 'clutter' being treated as 'bare ground'. Based on Figure 12, we compared the ALB-based and DL method results obtained using the CM valuation index, as shown in Table 6. In the case of the comparison index, we chose overall accuracy (OA) and macro F1-score as our targets. Correspondingly, Table 7 presents a sample of the CM valuation index. Finally, Tables 8–10 present the CM results obtained using the ALB (Case 0), RGB (Case 1-9), and RGB*nl*-based (Case 2-9) methods.

Findings revealed that LCC mapping using DL methods can achieve higher accuracy than when using ALB-based methods, with DL methods improving by nearly 25% in terms of the OA and macro F1-score. The CM shows that these three LCC results are generally diagonally dominant, and demonstrate that LCC can be achieved to some degree, even with only ALB point cloud data. However, using only n and l values, distinguishing between 'bamboo' and 'tree' is impossible when using the ALB-based approach. In addition, because of the ALB-based LCC method's mapping rule for the targeted site

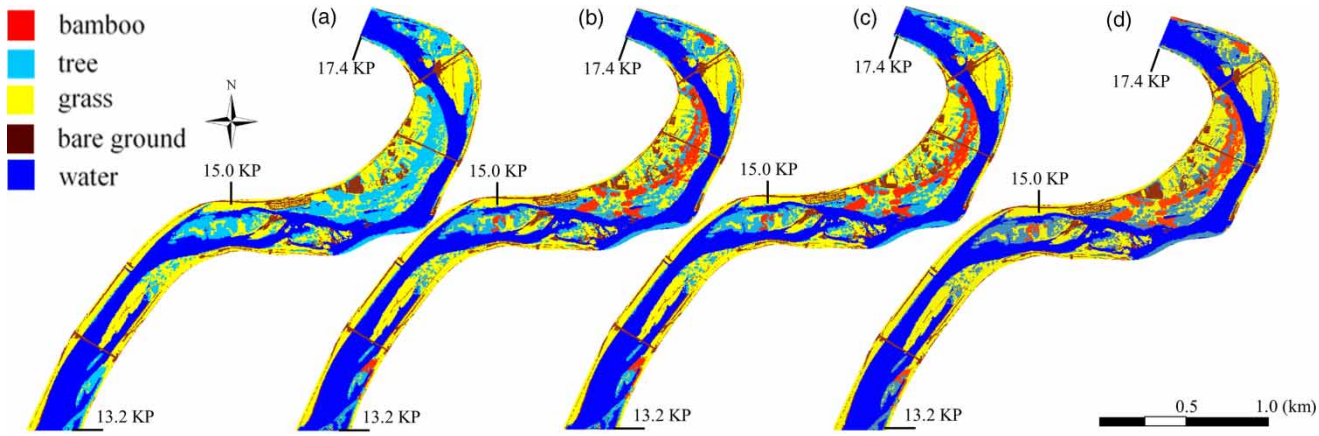

Figure 11 | Comparison of ALB-based results and DL method results for the whole area in November 2017: (a) Case 0 result, (b) Case 1-9 result, (c) Case 2-9 result, and (d) true label.

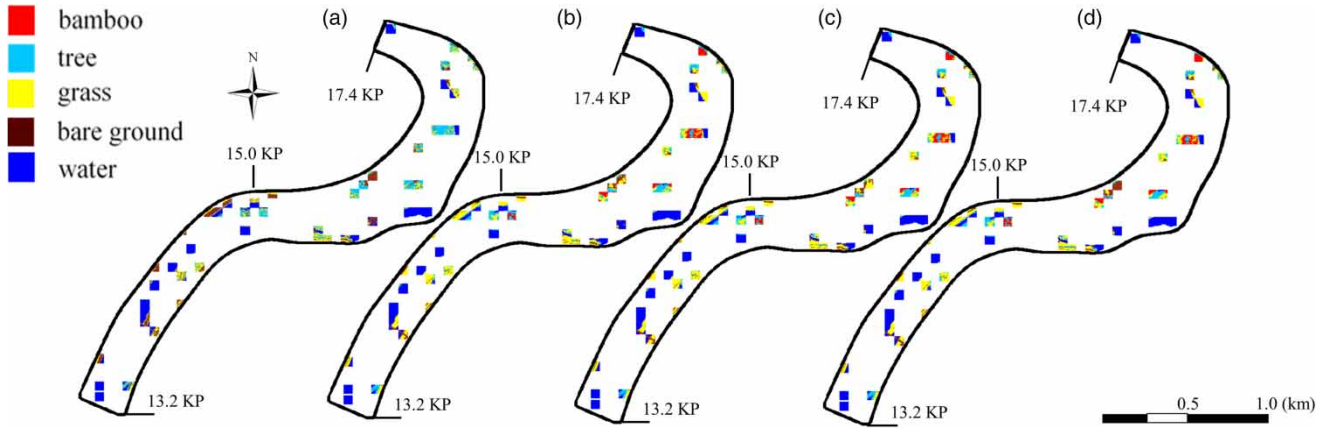

Figure 12 | Comparison of ALB-based result and DL methods results for the test area in November 2017: (a) Case 0 result, (b) Case 1-9 result, (c) Case 2-9 result, and (d) true label.

Table 6 | Confusion matrix (test area) of ALB- (Case 0), RGB- (Case 1-1), and RGB*nl*-based (Case 1-9) result

Confusion matrix valuation index

Symbol	Definition	Formula
Precision (X)	The ratio of the pixels for correctly predicted as X to all the pixels predicted as X	TP-X/PR-X
Recall (X)	The ratio of the pixels for correctly predicted as X to all the pixels true label as X	TP-X/TL-X
F1-score (X)	F1-score is the weighted average of Precision and Recall	2 * Precision (X) * Recall (X)/(Precision (X)+ Recall (X))
OA	Overall accuracy value of the confusion matrix	∑ TP-X/Amount of total pixels
Macro F1	Macro F1 is the average of all F1-score	∑ F1-score (X)/amounts of labels

X or Y includes five labels (B: Bamboo, T: Tree, G: Grass, BG: Bare Ground, W: Water).
TP-X is the amount of the pixels where true label and prediction are all X.
PR-X is the amount of the pixels where prediction is X.
TL-X is the amount of the pixels where true label is X.

Table 7 | Sample of confusion matrix valuation indices

	B	T	G	BG	W	Total	Recall (%)
B	TP-B	E-B/T	E-B/G	E-B/BG	E-B/W	TL-B	TP-B/TL-B
T	E-T/B	TP-T	E-T/G	E-T/BG	E-T/W	TL-T	TP-T/TL-T
G	E-G/B	E-G/T	TP-G	E-G/BG	E-G/W	TL-G	TP-G/TL-G
BG	E-BG/B	E-BG/T	E-BG/G	TP-BG	E-BG/W	TL-BG	TP-BG/TL-BG
W	E-W/B	E-W/T	E-W/G	E-W/BG	TP-W	TL-W	TP-W/TL-W
Total	PR-B	PR-T	PR-G	PR-BG	PR-W	Total pixels	
Precision (%)	TP-B/PR-B	TP-B/PR-T	TP-B/PR-G	TP-B/PR-BG	TP-B/PR-W		
OA, Macro F1							

E-X/Y: Amount of the pixels where true label is X, prediction is Y.

Table 8 | Accuracy valuation for Case 0 LCC (2 m resolution test area ALB-based result)

	B+T	G	BG	W	Total	Recall (%)
B+T	2,216	486	247	61	3,010	73.62
G	656	1,998	1,301	178	4,133	48.34
BG	81	276	793	79	1,229	64.52
W	16	46	315	5,045	5,422	93.05
Total	2,969	2,806	2,656	5,363	13,794	
Precision (%)	74.64	71.20	29.86	94.07		
OA = 0.73, Macro F1 = 0.67.						

Table 9 | Accuracy valuation for Case 1-9 LCC (2 m resolution test area RGB-based result)

	B	T	G	BG	W	Total	Recall (%)
B	998	12	0	214	5	1,229	81.20
T	16	1,692	29	198	11	1,946	86.95
G	0	142	875	47	0	1,064	82.24
BG	113	153	46	3,805	16	4,133	92.06
W	11	40	1	15	5,355	5,422	98.76
Total	1,138	2,039	951	4,279	5,387	13,794	
Precision (%)	87.70	82.98	92.01	88.92	99.41		
OA = 0.92, Macro F1 = 0.89.							

(Yoshida *et al.* 2020), grasses less than 30 cm tall are regarded as bare ground. For that reason, distinguishing 'grass' from 'bare ground' might be difficult. Furthermore, because of the 'salt and pepper effect', ALB-based method LCC mappings were not highly accurate in reproducing the corresponding TL mapping.

Table 10 | Accuracy valuation for Case 2-9 LCC (2 m resolution test area RGBnl-based result)

	B	T	G	BG	W	Total	Recall (%)
B	925	7	0	294	3	1,229	75.26
T	20	1,608	49	242	27	1,946	82.63
G	0	119	893	52	0	1,064	83.93
BG	133	123	40	3,815	22	4,133	92.31
W	9	25	0	19	5,369	5,422	99.02
Total	1,087	1,882	982	4,422	5,421	13,794	
Precision (%)	85.10	85.44	90.94	86.27	99.04		

OA = 0.91, Macro F1 = 0.88.

Case 1: RGB-based method

Case 1-1 to Case 1-9 from Figure 13 shows the confusion matrix relevant evaluation index (i.e. OA and macro F1-score) for the results obtained using the RGB-based method. The indexes are more prominent when the data from the same period are trained and inferred (Cases 1-1, 1-5, and 1-9). In contrast, when training and inferring data from different periods (Cases 1-2, 1-3, 1-4, 1-6, 1-7, and 1-8), the classification performance deteriorated, possibly because of differences in colouration between periods. For example, when training using March data and inferring on July data, the 'tree' in March appears brown, with only branches, whereas 'bamboo' seems green. In addition, the effects of solar radiation, water quality, and wind waves might affect the classification performance. Figure 14 presents some examples of misclassification: (a) while a 'tree' in July has leaves and appears green, a 'tree' in July is incorrectly classified as a 'bamboo'; (b) this reason also applies to the case of November data; and (c) when training with July data and inferring March data, the 'bare ground' in July data looks brown, and the 'tree' and 'grass' in March data are inferred as 'bare ground' because they are dead.

Case 2 and case 3: RGB*nl*-based method

Based on results in Case 2, compared to the RGB-based method, the RGB*nl*-based approach is less effective at improving accuracy (OA, macro F1-score). The findings imply that ALB data in use do not contribute as much to classification performance as RGB data when using an additional module. Finally, Case 3-1, Case 3-2, and Case 3-3 demonstrated results of inferring data from March, July, and November using a combination of data from the three targeted periods. Results show a slight decrease in accuracy when compared to Case 2-1, Case 2-5, and Case 2-9, which were trained and inferred during the same period. Therefore, it is preferable to train and infer using data from the same period rather than combining data from different periods to improve the classification performance. For reference, Cases 2-1/Case 2-4/Case 2-7, Case 2-2/Case 2-5/Case 2-8, and Case 2-3/Case 2-6/Case 2-9 showed training results and inferred data from the same or different periods for each of the three periods. When comparing these results to Cases 3-1, 3-2, and 3-3, it is apparent that we can improve classification performance when we have data from multiple periods by limiting it to a specific period and by using only data from that period. The findings also imply that using all available data can reduce the risk of degrading classification performance if data for the detailed period cannot be specified.

Application of inferred LCC results for 2018 Asahi River Flood simulation

To examine the applicability and efficacy of LCC predictions in estimating spatially distributed hydrodynamic roughness parameters (i.e. vegetation density values for different species), inferred LCC results based on the ALB-based and DL-based approaches were used for 2018 Asahi River flood modelling. The targeted flood records of observed water levels and the estimated discharge (based on a stage–discharge relation) at different hydraulic stations in the Asahi River were presented in an earlier report by Yoshida *et al.* (2021), revealing two peaks in the hydrograph observed during the flooding event, with peak discharge of 4,512 $m^3 s^{-1}$. According to the lower Asahi River flooding history, such flooding occurs approximately once every 40 years. For this study, we used a depth-averaged numerical approach with a steady-state flow condition for the

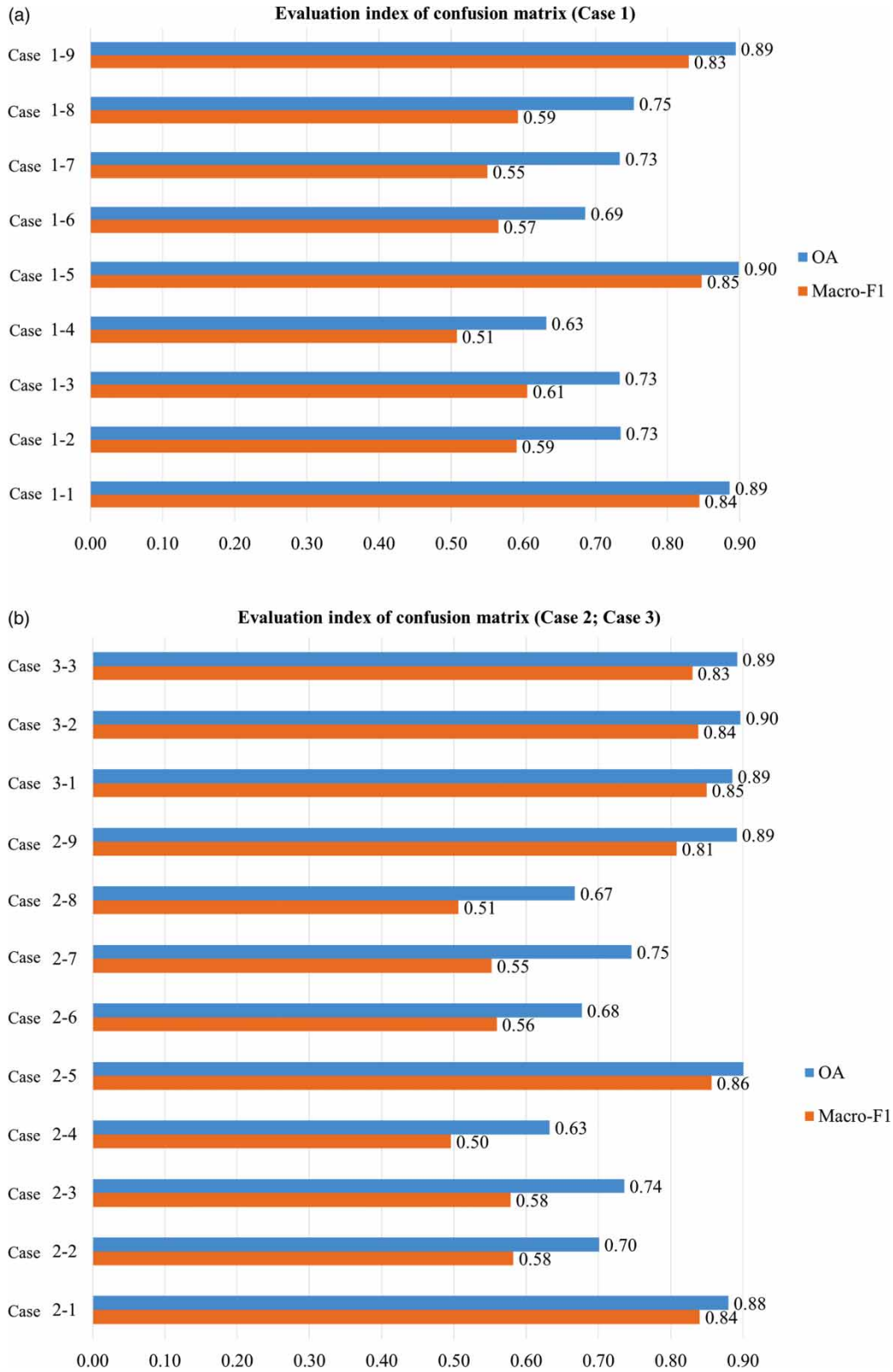

Figure 13 | Relevant evaluation index of the confusion matrix.

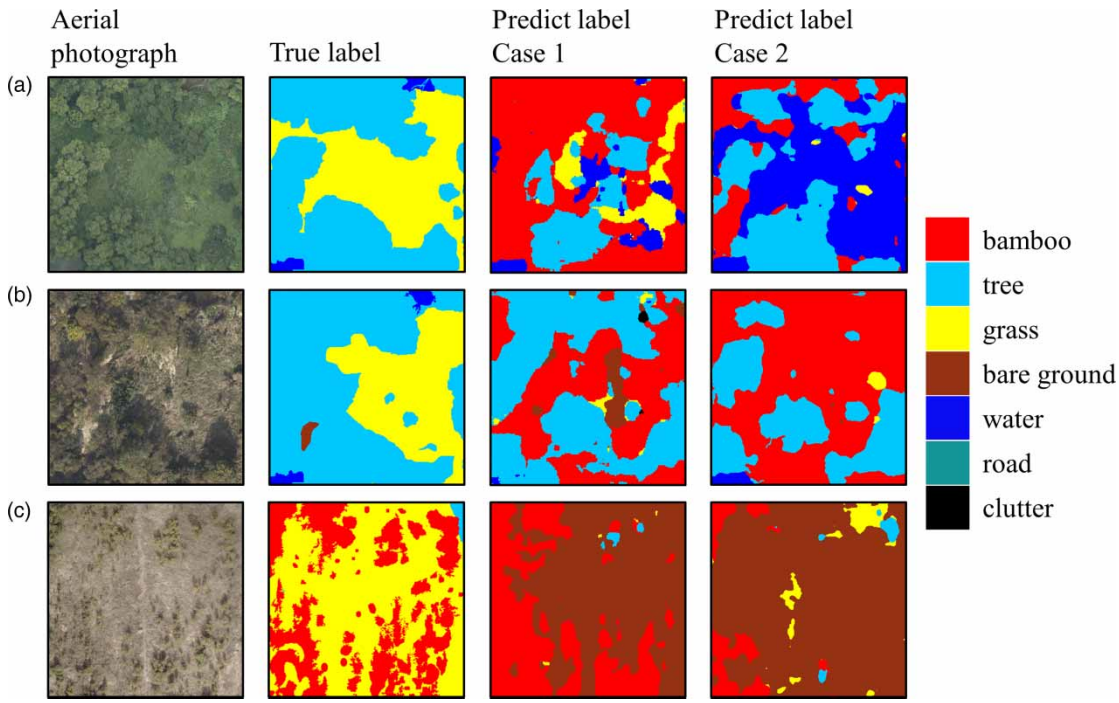

Figure 14 | Predicted label results for the specified area in targeted periods: (a) July, (b) November, and (c) March 2017.

peak flood simulation using a boundary-fitted coordinate system (Yoshida *et al.* 2021). In the earlier study (Yoshida *et al.* 2021), researchers revealed that simulated findings were reasonably consistent with observation results when the roughness parameters attributable to distributed vegetation were derived from ALB data, resulting in no significant uncertainty in longitudinal water level predictions. The researchers also demonstrated that distinguishing between the dominant species (e.g., woody vegetation and bamboo grove) in the river studied herein was challenging using an unsupervised LCC method based on ALB datasets alone. Consequently, such a misclassification could significantly impact flow-resistance parameterization estimation, affecting the spatial distribution of water levels and depth-averaged flow velocities. Furthermore, because the previous study (Yoshida *et al.* 2021) demonstrated that no substantial deformation occurred during the targeted flooding, we did not consider transient changes in bed elevation in hydrodynamic modelling. The time increment in the current study was 0.05 s, and the computational mesh for the Asahi River was composed of 434 × 57 cells with an average size of 10 m, representing 434 cross-sections and 57 nodes in each cross-section. The upstream boundary condition was determined using the estimated river discharge at Shimomaki Hydraulic Station (19 KP), whereas flood marks at the peak stage defined the downstream boundary condition at 13.2 KP. Based on earlier research by Maeno *et al.* (2005), Manning's roughness coefficient values were set as 0.028 and 0.026, respectively, for the main channel and floodplains. For this simulation, the drag forces for the targeted vegetation species were estimated using the term of $0.5\rho\lambda C_D l_{\min} u^2$, where ρ stands for water density, λ represents the vegetation density, C_D is the drag coefficient, $l_{\min} = \min\{h, l\}$ denote the minimum value of vegetation height l and local flow depth h, and u expresses represents the local flow velocity. Additionally, we assigned the drag coefficient value of 1 (Yoshida *et al.* 2021) for the current flood flow simulation. Table 11 presents the computational conditions used in the current 2D flood flow simulation and the density values of the targeted vegetation species in this study. Furthermore, during the field survey, only herbaceous species were observed under bridges crossing the targeted Asahi River. The presence of such vegetation might have a negligible effect on flow-resistance parameterization. Consequently, areas with bridges were treated as bare ground for this study.

Processing of inferred LCC results for flood simulation

As shown in Figure 15, after the pre-processing of step A and inference of step B, we obtained the 0.2 m pixel-based mesh LCC mapping from 13.2 to 17.4 KP. Simultaneously, mesh transformation is necessary if the inferred results in a square mesh are

Table 11 | Parameters used in the flood simulation 2D shallow water model

Simulation mesh	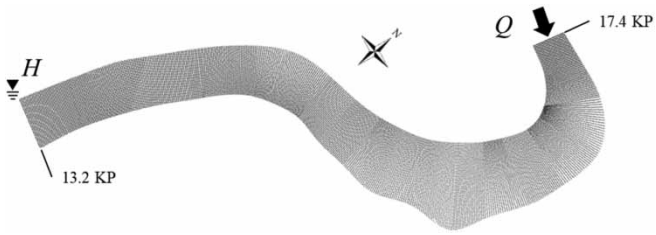		
	Mesh Number	Longitudinal: 434 Cross-sectional: 57	
Discrete Interval	Time step	$\Delta t = 0.05$ s	
	Spatial interval	$\Delta x = \Delta y = 10$ m	
Vegetation	Vegetation Density λ (m^{-1})	Tree (trunk)	0.013 ($l > 5$)[a], 0.023 ($0 < l \leq 0$)[b]
		Bamboo	0.286[a]
		Grass	0.031[a]
	Drag coefficient C_D		1.0
Manning roughness coefficient ($m^{-1/3}$ s^{-1})			Low water (main channel): 0.028, floodplain: 0.026
River discharge (at peak stage)			$Q = 4{,}251$ (m^3 s^{-1})
Downstream water level (at peak stage)			Asahi River 13.2 KP: $H = 10.67$ m

[a]Values proposed by Maeno *et al.* (2005).
[b]Values suggested by Shimizu *et al.* (2000).

to be used as flooding simulation parameters in a boundary-fitted mesh. In step C, the RGB-based and RGB*nl*-based methods inference can be transformed from a 0.2 m pixel-based mesh to a 2 m pixel-based mesh by considering the most frequently appearing labels. Then, using a 2 m simulation mesh that includes the LCC information (proceeding with steps D-1 and D-2), we transformed the information into 10 m simulation mesh via step E. Herein, for the flow-resistance parameterization, Sim-a was created using all the simulation mesh LCC information (ALB-based method), whereas Sim-b and Sim-c were generated, respectively, using RGB*nl*-based results and true label. Subsequently, as shown in step F (Figure 15), the inferred LCC results were transferred as input data for the 2018 Asahi River flood simulation (Figure 16).

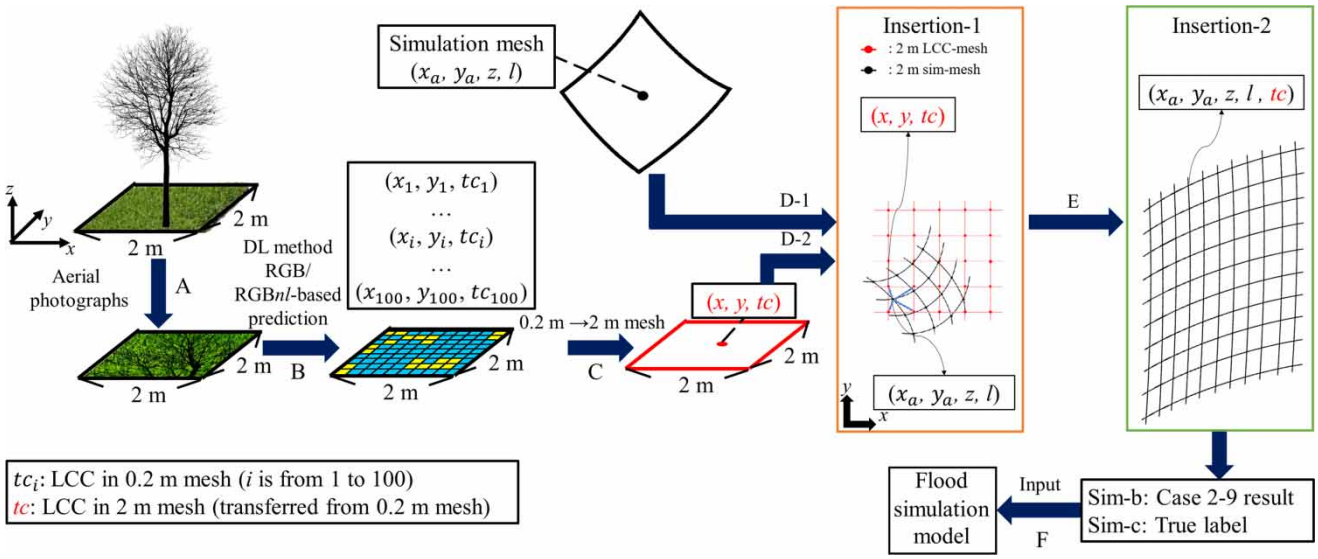

Figure 15 | Processing of transferring inferred LCC results for flood simulation.

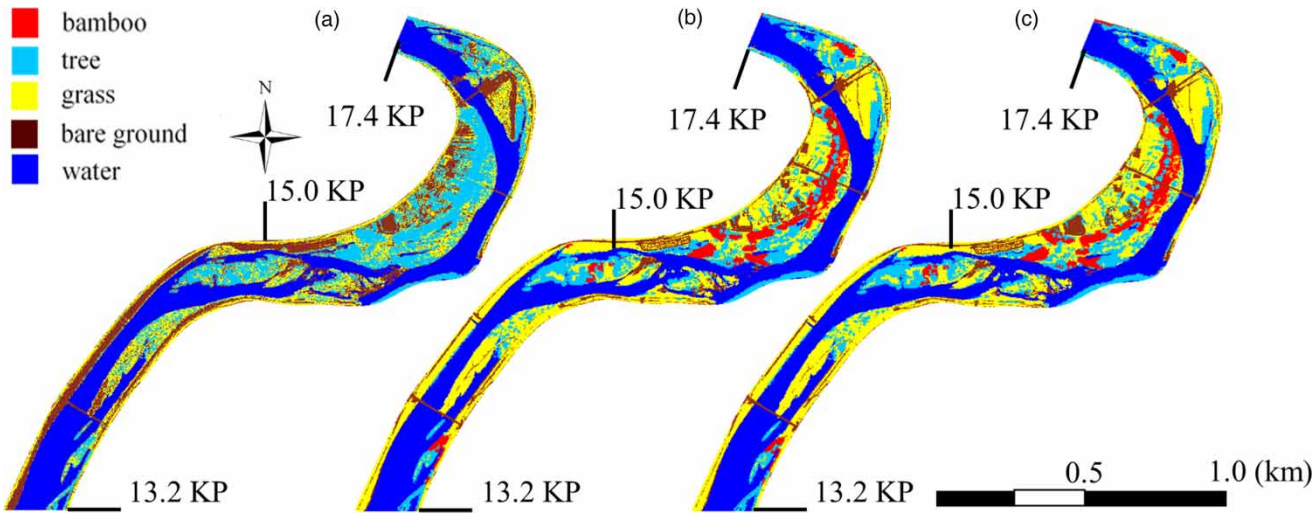

Figure 16 | Inferred LCC results for parameterization in flood simulation model: (a) Sim-a – ALB-based, Case 0 result, (b) Sim-b – RGB*nl*-based, Case 2-9 result, and (c) Sim-c – true label.

Flood simulation using LCC inference results

Figure 17 presents a comparison of simulated and observed water levels along the Asahi River's left-bank and right-bank reaches during the peak stage of the 2018 flooding. As benchmarked points, the figure also includes flood marks at the peak stage, the high water level (HWL), and the river embankment level along the targeted reaches. For the left-bank case (Figure 17(a)), simulated water levels using both the ALB-based and DL-based parameters were reasonably consistent with the referenced flood marks and the water level estimates based on images from closed-circuit television (CCTV). In contrast, in terms of residual sum of squares (RSS) values (Table 12), the DL-based simulation reproduced flood marks that were markedly better than the ALB-based simulation for the right-bank case (Figure 17(b)), thereby implying that the DL results outperformed the ALB results. Furthermore, Figure 18 depicts the flow velocity and water depth results estimated from the current flood simulation using flow-resistance parameters derived from the ALB-based and RGB*nl*-based LCC results. Those findings revealed that the simulated flow velocity and depth have differed considerably in both cases because of differences in land cover between the targeted ALB-based and RGB*nl*-based LCC results. For example, at location b (Figure 18), the RGB*nl*-based water velocity varied markedly from the ALB-based results because the DL method correctly distinguished the dominant bamboo grove from woody species in the targeted area. Overall, the numerically simulated results have demonstrated the importance of high-accuracy LCC mapping in hydraulic engineering tasks.

CONCLUSION AND FUTURE RESEARCH DIRECTIONS

Results revealed that the DL methods outperformed the ALB-based method in terms of typical valuation indexes. In this study, three seasonal datasets with different leafy conditions (i.e. no–leaf and leaf–on) significantly influenced LCC results, demonstrating that use of the same period datasets for the different trained and test areas yielded higher accuracy. Currently used datasets with shorter time variations of around 3 months might limit our results because longer periods datasets supposedly provide better predictions using the DL approach. Furthermore, the depth-averaged flood simulation model showed that the water level inferred using the DL-based method much more closely approximated the observed water level than the conventionally used ALB-based approach did. In addition, the flow velocity and water depth inferred from the DL method results differed from those inferred from ALB-based LCC results because of changes in the classification of the most dominant riparian vegetation species in the targeted region: trees and bamboo. In addition, although the RGB*nl*-based method includes ALB-derived voxel-based laser points and vegetation height information, the LCC mapping accuracy has not improved markedly over the RGB-based approach. Overall, these findings might compel us to revise our model for use in future studies, considering additional processed attributes from ALB datasets (i.e. reflection intensity from DTM and DSM) and using a few more inputs to the original DL model in addition to RGB. To conclude, the results of this study are expected to support reasonable engineering measures for flood control in vegetated rivers. Finally, based on our current findings, we recommend

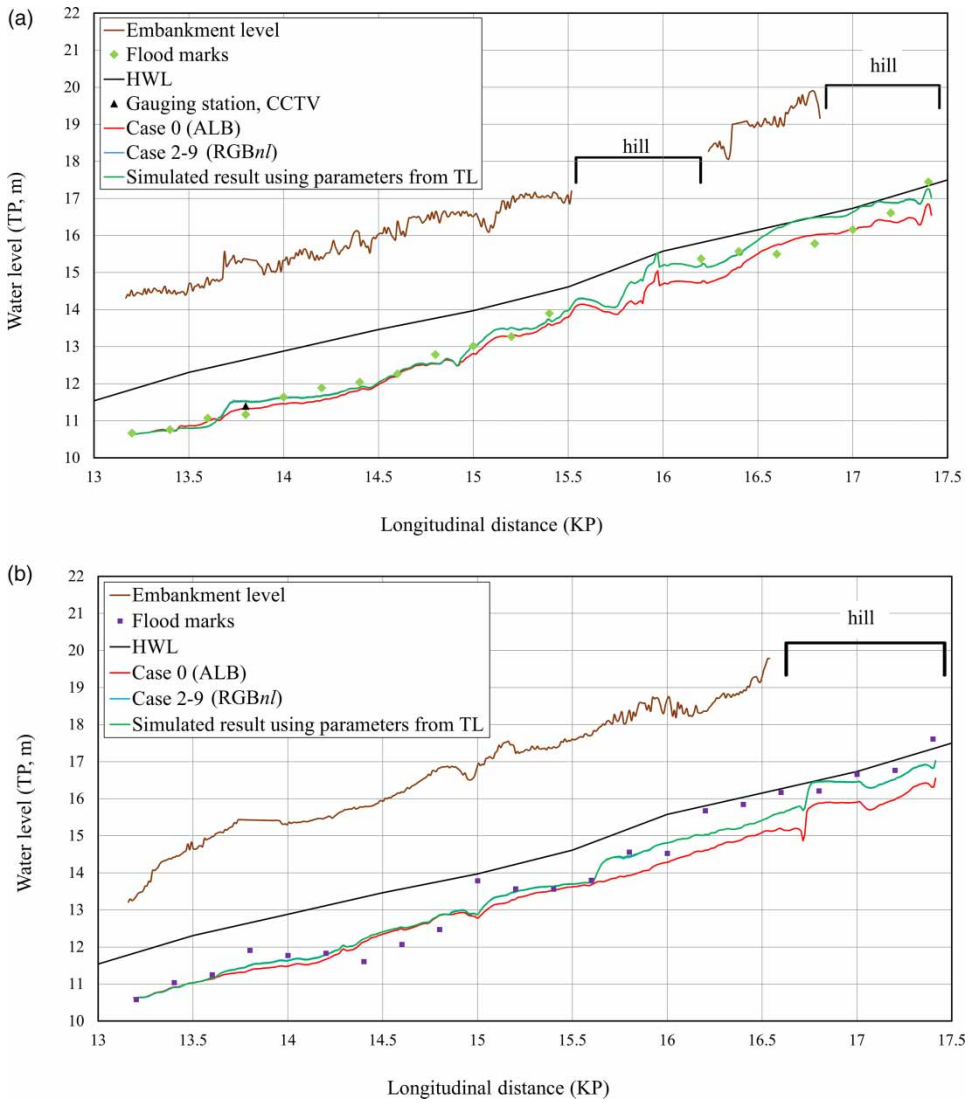

Figure 17 | Water level estimated from flood simulation results obtained using parameters of different LCC methods: (a) left-bank side and (b) right-bank side. HWL and TL stand for high water level and true label, respectively.

Table 12 | RSS of the different LCC method results comparing with flood marks

	RSS (m^2)		
	$\sum(h_{ALB}-h_{FM})^2$	$\sum(h_{RGBnl}-h_{FM})^2$	$\sum(h_{TL}-h_{FM})^2$
Left-bank side	1.58	1.77	1.73
Right-bank side	8.49	3.68	3.70

RSS: Residual sum of squares; FM: Flood marks.
h_{ALB}: Water level at flood mark using ALB-based result.
h_{RGBnl}: Water level at flood mark using RGB*nl*-based result.
h_{TL}: Water level at flood mark using True label.
h_{FM}: Field observation of water level at flood mark.

conducting comprehensive research investigating balanced riparian ecosystems conservation. Furthermore, because of higher cost in ALB data acquisition and recent advances in remote sensing technologies, we intend to use cost-effective unmanned aerial vehicle-borne LiDAR-derived data (Islam *et al.* 2021) for future relevant research due to its convenience of more

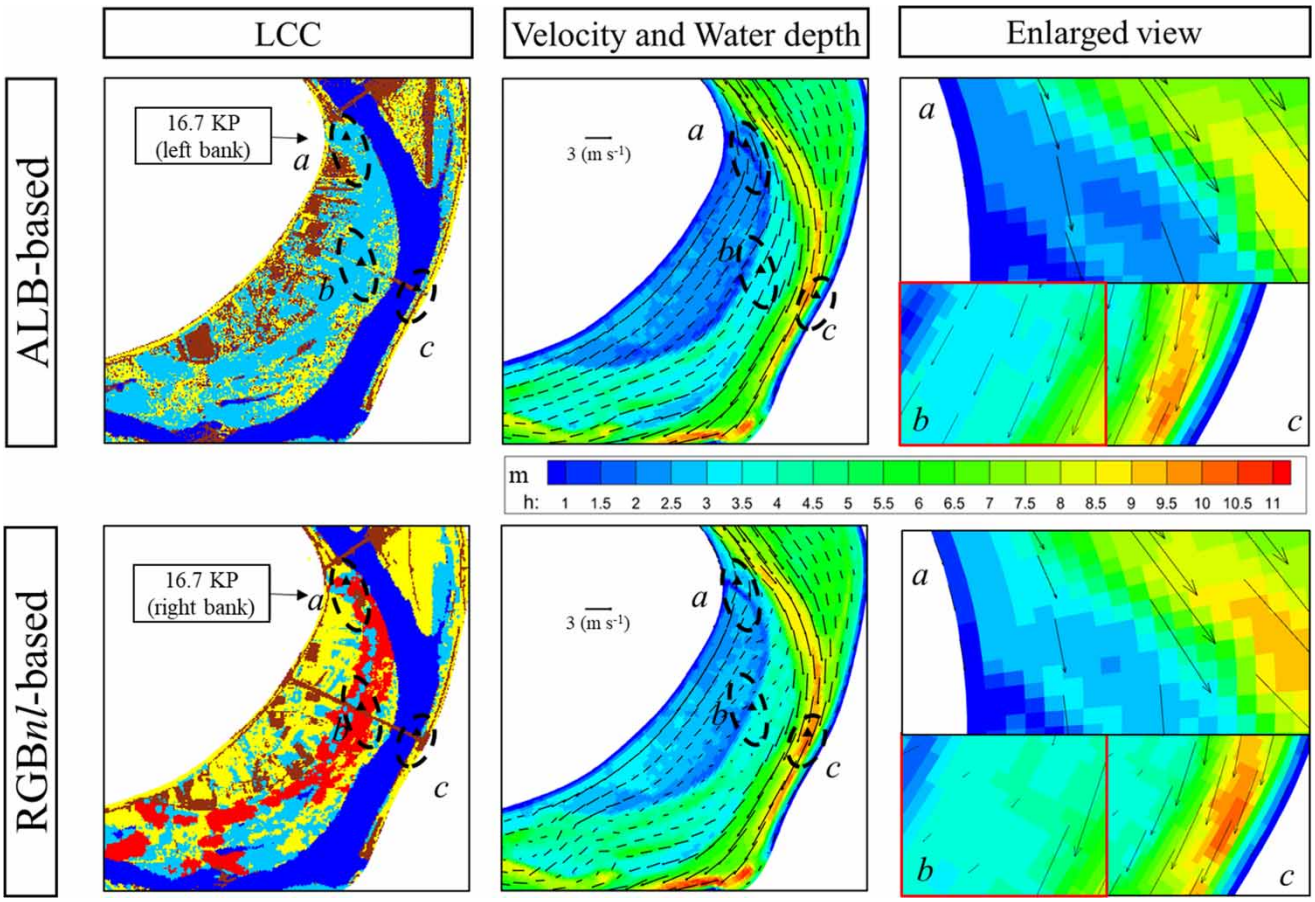

Figure 18 | Velocities and water levels inferred from flood simulation using parameters of ALB-based and RGB*nl*-based results with LCC.

detailed point density and concurrently captured high spatial resolution aerial images. In addition, because sedimentation can change the LCC and roughness of rivers (Pinho *et al.* 2020), it is recommended to identify such factors using RGB analysis and the well-proven ALB technique, which can aid in identifying potential uncertainty in hydrodynamic-numerical modelling.

ACKNOWLEDGEMENTS

The authors thank both the Chugoku Regional Development Bureau, Ministry of Land, Infrastructure, Transport and Tourism, Japan and Pasco Corp. for offering necessary data recorded along the Asahi and Hyakken rivers. The authors are also grateful to the dedicated support of Mr Nomura in conducting true label data production for this work. The authors would also like to express their gratitude to the anonymous reviewers for their useful suggestions on the manuscript.

FUNDING

This study was supported in part by the Chugoku Kensetsu Kousaikai, the Wesco Scientific Promotion Foundation and the Japan Society for the Promotion of Science (JSPS) KAKENHI [grant 18K04370].

DATA AVAILABILITY STATEMENT

Data cannot be made publicly available; readers should contact the corresponding author for details.

REFERENCES

Blaschke, T., Lang, S., Lorup, E., Strobl, J. & Zeil, P. 2000 Object-oriented image processing in an integrated GIS/remote sensing environment and perspectives for environmental applications. *Environmental Information for Planning, Politics and the Public* **2**, 555–570.

Carbonneau, P. E., Dugdale, S. J., Breckon, T. P., Dietrich, J. T., Fonstad, M. A., Miyamoto, H. & Woodget, A. S. 2020 Adopting deep learning methods for airborne RGB fluvial scene classification. *Remote Sensing of Environment* **251**, 112107. https://doi.org/10.1016/j.rse.2020.112107.

Chen, L. C., Papandreou, G., Kokkinos, I., Murphy, K. & Yuille, A. L. 2017 DeepLab: semantic image segmentation with deep convolutional nets, atrous convolution, and fully connected CRFS. *IEEE Transactions on Pattern Analysis and Machine Intelligence* **40** (4), 834–848. https://doi.org/10.1109/TPAMI.2017.2699184.

Chen, L. C., Zhu, Y., Papandreou, G., Schroff, F. & Adam, H. 2018 Encoder-decoder with atrous separable convolution for semantic image segmentation. In: *Proceedings of the European Conference on Computer Vision (ECCV)*, pp. 801–818.

Chow, V. T. 1959 *Open-Channel Hydraulics*. McGraw-Hill, New York, NY.

Dargan, S., Kumar, M., Ayyagari, M. R. & Kumar, G. 2019 A survey of deep learning and its applications: a new paradigm to machine learning. *Archives of Computational Methods in Engineering* 1–22. https://doi.org/10.1007/s11831-019-09344-w.

Dimitriadis, P., Tegos, A., Oikonomou, A., Pagana, V., Koukouvinos, A., Mamassis, N., Koutsoyiannis, D. & Efstratiadis, A. 2016 Comparative evaluation of 1D and quasi-2D hydraulic models based on benchmark and real-world applications for uncertainty assessment in flood mapping. *Journal of Hydrology* **534**, 478–492. https://doi.org/10.1016/j.jhydrol.2016.01.020.

Do, H. T., Raghavan, V., Truong, L. X. & Yonezawa, G. 2019 Multi-scale object-based fuzzy classification for LULC mapping from optical satellite images. *Spatial Information Research* **27** (2), 247–257. https://doi.org/10.1007/s41324-019-00240-w.

Fehérváry, I. & Kiss, T. 2020 Identification of riparian vegetation types with machine learning based on LiDAR point-cloud made along the lower Tisza's floodplain. *Journal of Environmental Geography* **13**, 53–61. https://doi.org/10.2478/jengeo-2020-0006.

Global floods 2021 IAHR experts call for science-informed action! International Association for Hydro-Environment Engineering and Research. Available from: https://www.iahr.org/index/detail/482.

Green, J. C. 2005 Modelling flow resistance in vegetated streams: review and development of new theory. *Hydrological Processes: An International Journal* **19** (6), 1245–1259. https://doi.org/10.1002/hyp.5564.

Islam, M. T., Yoshida, K., Nishiyama, S., Sakai, K. & Tsuda, T. 2021 Characterizing vegetated rivers using novel unmanned aerial vehicle-borne topo-bathymetric green lidar: seasonal applications and challenges. *River Research and Applications*. https://doi.org/10.1002/rra.3875.

Maeno, S., Watanabe, S. & Fujitsuka, Y. 2005 Improvement of modeling of flow analysis using easily obtained vegetation characteristics. *Journal of Hydraulic, Coastal and Environmental Engineering* **803**, 91–104 (in Japanese with English abstract). https://doi.org/10.2208/jscej.2005.803_91.

Mason, D. C., Cobby, D. M., Horritt, M. S. & Bates, P. D. 2003 Floodplain friction parameterisation in two-dimensional river flood models using vegetation heights derived from airborne scanning laser altimetry. *Hydrological Processes* **17** (9), 1711–1732. https://doi.org/10.1002/hyp.1270.

MLIT 2007 *River Flow Situation of the Asahi River and Water Quality, Ministry of Land, Infrastructure, Transport and Tourism, Japan*. Available from: https://www.mlit.go.jp/river/basic_info/jigyo_keikaku/gaiyou/seibi/asahi_index.html.

Nepf, H. M. 2012 Hydrodynamics of vegetated channels. *Journal of Hydraulic Research* **50** (3), 262–279. https://doi.org/10.1080/00221686.2012.696559.

Nikora, V., Larned, S., Nikora, N., Debnath, K., Cooper, G. & Reid, M. 2008 Hydraulic resistance due to aquatic vegetation in small streams: field study. *Journal of Hydraulic Engineering* **134** (9), 1326–1332. https://doi.org/10.1061/(ASCE)0733-9429(2008)134:9(1326).

Pinho, J. L., Vieira, L., Vieira, J. M. P., Venâncio, S., Simoes, N. E., Sa Marques, J. A. & Santos, F. S. 2020 Assessing causes and associated water levels for an urban flood using hydroinformatic tools. *Journal of Hydroinformatics* **22** (1), 61–76. https://doi.org/10.2166/hydro.2019.019.

Ronneberger, O., Fischer, P. & Brox, T. (2015, October) U-net: Convolutional networks for biomedical image segmentation. In: *International Conference on Medical image computing and computer-assisted intervention*. pp. 234–241. Springer, Cham. https://doi.org/10.1007/978-3-319-24574-4_28.

Shih, S. S. & Chen, P. C. 2021 Identifying tree characteristics to determine the blocking effects of water conveyance for natural flood management in urban rivers. *Journal of Flood Risk Management*, e12742. https://doi.org/10.1111/jfr3.12742.

Shimizu, Y., Kobatake, S. & Arafune, T. 2000 Numerical study of the flood-flow stage in gravel-bed river with the excessive riverine trees. *Annual Journal of Hydraulic Engineering* **44**, 819–824. (in Japanese with English abstract).

Straatsma, M. W. & Baptist, M. J. 2008 Floodplain roughness parametrisation using airborne laser scanning and spectral remote sensing. *Remote Sensing of the Environment* **112**, 1062–1080. https://doi.org/10.3390/rs9111101.

Sun, X., Shiono, K., Rameshwaran, P. & Chandler, J. H. 2010 Modelling vegetation effects in irregular meandering river. *Journal of Hydraulic Research* **48** (6), 775–783. https://doi.org/10.1080/00221686.2010.531101.

Tian, L., Qu, Y. & Qi, J. 2021 Estimation of forest LAI using discrete airborne LiDAR: a review. *Remote Sensing* **13** (12), 2408. https://doi.org/10.3390/rs13122408.

Vetter, M., Höfle, B., Hollaus, M., Gschöpf, C., Mandlburger, G., Pfeifer, N. & Wagner, W. 2011 Vertical vegetation structure analysis and hydraulic roughness determination using dense ALS point cloud data – a voxel based approach. *International Archives of Photogrammetry, Remote Sensing and Spatial Information Sciences* **38** (5). https://doi.org/10.5194/isprsarchives-XXXVIII-5-W12-265-2011.

Wei, K., Ouyang, C., Duan, H., Li, Y., Chen, M., Ma, J., An, H. & Zhou, S. 2020 Reflections on the catastrophic 2020 Yangtze River Basin flooding in southern China. *The Innovation* **1** (2), 100038. https://doi.org/10.1016/j.xinn.2020.100038.

Yoshida, K., Maeno, S., Mano, K., Iwaki, T., Ogawa, S. & Akoh, R. 2017 Determination method for vegetation species distribution in rivers using airborne laser bathymetry. *Journal Japan Society of Civil Engineers, Series A2 (Applied Mechanics)* **73** (2), I_607–I_618. (in Japanese with English abstract). https://doi.org/10.2208/jscejam.73.I_607.

Yoshida, K., Maeno, S., Ogawa, S., Mano, K. & Nigo, S. 2020 Estimation of distributed flow resistance in vegetated rivers using airborne topo-bathymetric LiDAR and its application to risk management tasks for Asahi River flooding. *Journal of Flood Risk Management* **13** (1), e12584. https://doi.org/10.1111/jfr3.12584.

Yoshida, K., Nagata, K., Maeno, S., Mano, K., Nigo, S., Nishiyama, S. & Islam, M. T. 2021 Flood risk assessment in vegetated lower Asahi River of Okayama Prefecture in Japan using airborne topo-bathymetric LiDAR and depth-averaged flow model. *Journal of Hydro-Environment Research*. https://doi.org/10.1016/j.jher.2021.06.005.

Yu, Q., Gong, P., Clinton, N., Biging, G., Kelly, M. & Schirokauer, D. 2006 Object-based detailed vegetation classification with airborne high spatial resolution remote sensing imagery. *Photogrammetric Engineering & Remote Sensing* **72** (7), 799–811. https://doi.org/10.14358/PERS.72.7.799.

First received 13 October 2021; accepted in revised form 27 December 2021. Available online 19 January 2022